Measurements on a Yawed Model Rotor Blade Pitching in Reverse Flow

Luke R. Smith[1], Andrew H. Lind[2], and Anya R. Jones[3]

[1]Graduate Research Assistant, University of Maryland, College Park
[2]Assistant Research Engineer, University of Maryland, College Park
[3]Associate Professor, University of Maryland, College Park

In forward flight, high advance ratio rotors encounter a large region of reverse flow on their retreating side. The reverse flow region is dominated by the reverse flow dynamic stall vortex (RFDSV), which incurs large unsteady torsional loads that are not well-predicted by modern comprehensive rotorcraft codes. To gain a physical understanding of the impact of yaw on the RFDSV, a sub-scale, NACA0012 model rotor blade has been experimentally tested at two reverse flow yaw angles, Λ_{rev} = 0° and Λ_{rev} = 30°, over a range of reduced frequencies, 0.160$< k <$0.450. Pressure time histories were obtained from surface-mounted unsteady pressure transducers, and three-component velocity fields were obtained using time-resolved stereoscopic particle image velocimetry at the midspan. The present work focuses on the impact of yaw on general flow morphology, dynamic stall vortex behavior, and spanwise flow. The presence of yaw was found to lessen the magnitude of the pressure wave induced by the RFDSV and hinder the development of secondary flow structures. The presence of yaw did not lead to a noticeable difference in the convection speed of the RFDSV in the direction of the freestream, but did lead to a substantially higher magnitude of spanwise flow. Ultimately, this experimental study lays the groundwork for understanding three-dimensional effects on the formation and convection of the reverse flow dynamic stall vortex.

Nomenclature

Λ	Forward flow yaw angle, deg
α	Forward flow angle of attack, deg
c_{g}	Geometric chord, in
c_{e}	Effective chord, in
R	Rotor radius, in
r	Spanwise radial location, in
ψ	Azimuthal position, deg
k	Reduced frequency
s	Reduced time
T	Period of pitch cycle, sec
μ	Rotor advance ratio
f	Blade pitching frequency, Hz
V_{loc}	Local velocity, m/sec
Λ_{rev}	Reverse flow yaw angle, deg
α_{rev}	Reverse flow angle of attack, deg
α_{rev}	Reverse flow angle of attack, deg
$\alpha_{0,\mathrm{rev}}$	Reverse flow mean pitch angle, deg
$\alpha_{1,\mathrm{rev}}$	Reverse flow pitch amplitude, deg
w	Spanwise component of velocity, m/sec
x/c	Non-dimensional distance along chord
z/c	Non-dimensional vertical distance
ω	Vorticity, rad/s
C_{P}	Local pressure coefficient

Presented at the 43rd European Rotorcraft Forum, in Milan, Italy in September 2017. Corresponding author e-mail address: lsmith1@umd.edu

1. INTRODUCTION

When a rotor operates at high advance ratio, a large portion of its retreating side is immersed in reverse flow, a complex aerodynamic environment with highly unsteady airloads [1]. The reverse flow dynamic stall vortex (RFDSV), a flow structure detected in both full-scale [2] and Mach-scale [3,4] rotors, has been identified as the dominant feature of the reverse flow region and is believed to be partly responsible for impulsive torsional loading on retreating side of high advance ratio rotors. The blade loads incurred by the RFDSV are not well-predicted by modern comprehensive rotorcraft codes [5], and in response, experimental work has been aimed at understanding the fundamental physics behind the formation and convection of the RFDSV. Prior work by the authors has characterized the RFDSV in sinusoidal [6] and linear [7] pitching but has been limited to 2D models of reverse flow. The purpose of this work is to begin investigating three dimensional effects by characterizing the impact of a static yaw angle Λ_{rev} on an airfoil undergoing dynamic pitching in reverse flow.

Prior research on yawed flow has focused on the "independence principle," the concept that forces on a blade in yawed flow are proportional to the square of the flow component parallel to the chord [8]. Purser and Spearman evaluated this notion by measuring the airloads on a variety of rigid airfoils held at static angles of attack and static yaw angles in forward flow [9]. They found that the independence principle is valid for attached flow, but observed a delay in lift stall to greater angles of attack with increasing yaw angle. Inspired by the validity of the independence principle in attached flow, Harris [10] and Gormont [8] proposed that the effect of yaw on a rotor blade section could be modeled with static corrections to existing airfoil tables, but these corrections do not account for dynamic pitching of a rotor blade in forward flight.

To evaluate the impact of yaw on the dynamic stall regime, St Hilaire et al., as part of a comprehensive study by UTRC, evaluated a dynamically pitching NACA 0012 airfoil in forward flow at Λ = 0° and Λ = 30°, varying the mean pitch angle from 0° to 15° and the pitch amplitude from 8° to 10°. Analyzing pressure measurements along the airfoil chord, the authors reached two important conclusions: first, the addition of yaw delays the onset of dynamic stall to a later time in the pitching cycle [11], and second, the delay in dynamic stall can be attributed to reduced convection speed of the dynamic stall vortex in yawed flow [12]. Leishman, in a semi-empirical analysis of past experimental data sets, theorized that yawed flow delays dynamic stall primarily by altering flow near the trailing edge separation point, and his subsequent modeling effort produced close agreement with the experimental results [13].

The present work seeks to assess whether the impacts of yaw on forward flow dynamic stall hold in reverse flow, where the mechanism for vortex formation is fundamentally different than forward flow [6]. The present work considers a NACA 0012 airfoil pitching at two static reverse flow yaw angles, Λ_{rev} = 0° and Λ_{rev} = 30°, and employs unsteady pressure transducers along the model surface and stereoscopic particle image velocimetry to capture time-resolved flow fields. The experiments presented here focus on the identification of dominant flow features, the behavior of these flow features after their formation, and the amount of spanwise flow in each configuration. This work is aimed toward developing a basic understanding of the three dimensional behavior of the RFDSV.

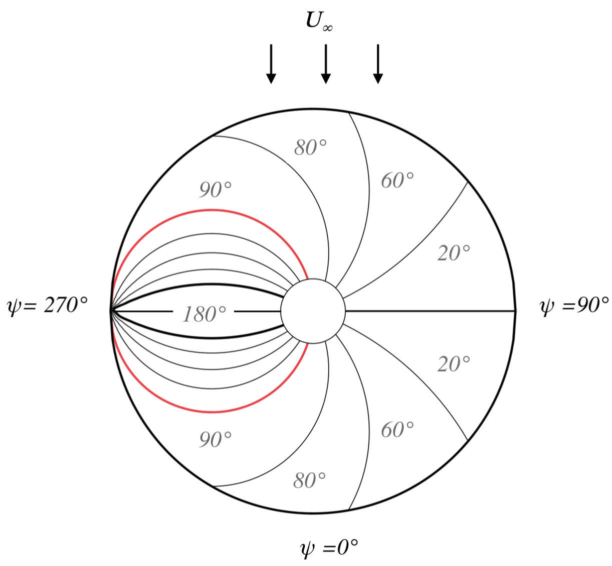

Fig. 1: Top-down view of rotor at μ = 1.0 with iso-contour lines of yaw angle. The bounds of the reverse flow region are highlighted in red. Adapted from [14].

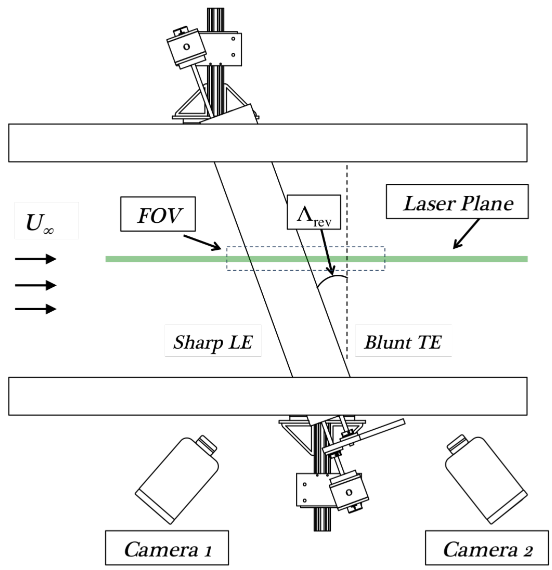

Fig. 2: Experimental setup in the 20 x 28 in low speed wind tunnel at the University of Maryland. The field of view (FOV) is shown at the midspan of the tunnel.

2. METHODOLOGY

The yaw angle of a blade element is defined as the angle between the local velocity vector and the chord line, and is dependent upon radial position, azimuthal position, and advance ratio [15]. Figure 1 shows theoretical iso-contours of yaw angle on a rotor operating at μ = 1.0, illustrating the wide range of yaw angles encountered by a blade element in forward flight. The reverse flow region is outlined in red and involves a rapid sweep of yaw angle over the region $90° < \Lambda < 180°$. For convenience, this work de-

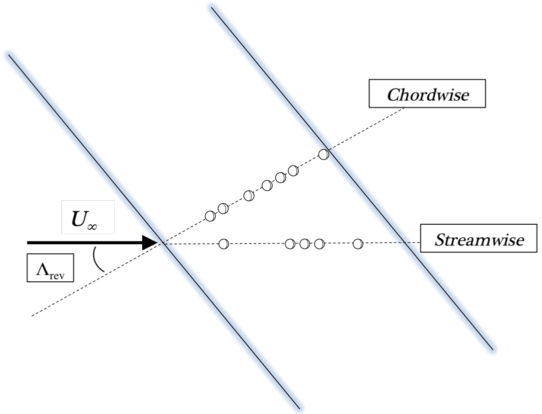

Fig. 3: Defintion of the streamwise and chordwise directions. Streamwise sensors are used in the yawed configuration, and chordwise sensors are used in the unyawed configuration.

	Chordwise x/c	Streamwise x/c
Sensor 1	0.2121	0.2215
Sensor 2	0.2798	0.5049
Sensor 3	0.4495	0.5661
Sensor 4	0.5354	0.6273
Sensor 5	0.6061	0.8644
Sensor 6	0.6768	—
Sensor 7	1.000	—

Fig. 4: Non-dimensional sensor locations in each direction. Note that x/c = 0 corresponds to the sharp leading edge and x/c = 1.0 corresponds to the blunt trailing edge.

fines the reverse flow yaw angle, Λ_{rev}, according to Equation 1, making Λ_{rev} relative to airfoil's geometric trailing edge.

$$\Lambda_{\mathrm{rev}} = 180^\circ - \Lambda \tag{1}$$

With the wide range of yaw angles in mind, the present work models a rotor blade element in reverse flow as a dynamically pitching infinite blade held at two static yaw angles in reverse flow, $\Lambda_{\mathrm{rev}} = 0^\circ$ and $\Lambda_{\mathrm{rev}} = 30^\circ$. Experiments were performed in a 20 x 28 in low speed, open loop wind tunnel at the University of Maryland on an aspect ratio 4 NACA0012 airfoil model. Figure 2 shows the experimental setup. A rigid model rotor blade was constructed from acrylic plastic with a geometric chord of 5 in, and outfitted with a primary 0.375 in stainless steel spar at the geometric quarter chord and a secondary 0.25 in stainless steel spar at the geometric 60% chord. A programmable servo motor, coupled with a four-bar linkage system, allowed for the dynamic pitching of the model blade about its geometric quarter chord. Static yaw angles were achieved by attaching a housing structure to the primary spar and fixing the housing structure atop and below the wind tunnel. A rotary encoder mounted to the primary spar recorded time-resolved angle of attack data.

2.1 Data Acquisition

The experimental setup involved the collection of two types of data: time-resolved velocity fields from stereoscopic particle image velocimetry (PIV) and pressure time histories from surface-mounted unsteady pressure transducers. When performing stereoscopic PIV, a high-speed laser, operating at frequencies ranging from 200-500 Hz, illuminated a plane at the midspan of the wind tunnel in both the yawed and unyawed configuration. Two high-speed 4 Mpx cameras were placed beneath the wind tunnel test section and faced toward the suction surface of the pitching airfoil. The cameras were tilted relative to the vertical and positioned such that both cameras achieved approximately the same field of view, allowing the out-of-plane velocity component to be resolved in overlapping regions. A PivLight40 Series Aerosol Generator produced 1 μm tracer particles at a rate of 5.0 x 10^8 particles/sec. Due to difficulties in achieving uniform seeding at high Reynolds numbers, the stereo PIV experiments were performed at a test Reynolds number of Re = 2.5 x 10^4.

It is important to note that in both the yawed and unyawed configurations, the laser plane was aligned with the freestream direction, parallel to the tunnel ceiling and floor. In the unyawed configuration, the laser sheet illuminates a section parallel to the airfoil's chordwise direction. In the yawed configuration, the laser sheet illuminates a section tilted from the airfoil's chordwise direction. Figure 3 illustrates the laser plane direction when the blade is yawed. In all future sections, the term "chordwise" refers to the orientation of the laser plane in the unyawed configuration, and the term "streamwise" refers to the orientation of the laser plane in the yawed configuration. The effective chord in the streamwise direction is larger than the effective chord in the chordwise direction.

Figure 3 also illustrates the placement of chordwise and streamwise unsteady pressure transducers along the airfoil suction surface. Endevco pressure transducer chips were mounted to custom-designed circuit boards [3], calibrated in a controlled vacuum chamber, and installed within a 3D printed section at the midspan of the model rotor blade. Figure 4 gives non-dimensional locations of the pressure sensors relative to the sharp aerodynamic leading edge of the airfoil. Note that chordwise and streamwise

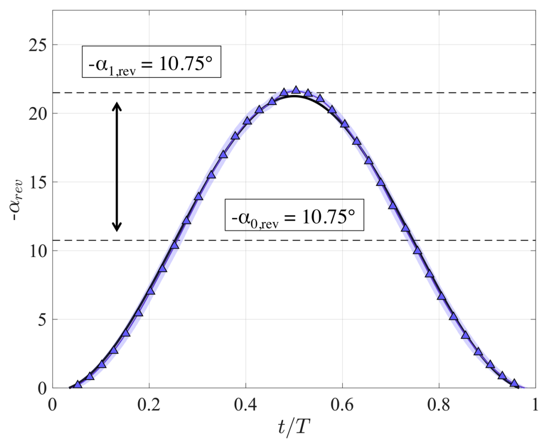

Fig. 5: Pitching kinematics for the k = 0.217 baseline case, phase-averaged over 120 cycles. The resulting kinematics show little variation compared to a perfect sinusoidal fit.

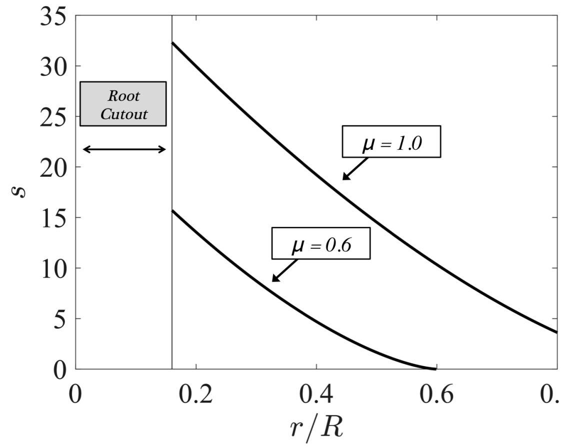

Fig. 6: Reduced time distribution along rotor radius for a rotor with R = 40 in., c = 3.15 in., and Ω = 900 RPM passing through reverse flow.

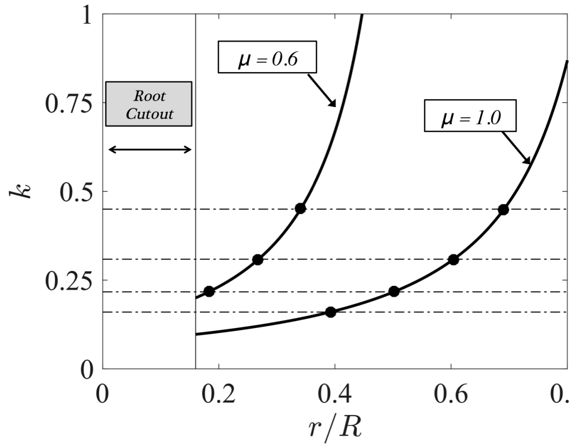

Fig. 7: Effective reduced frequency distribution along rotor radius for a rotor with R = 33.5 in., c = 3.15 in., and Ω = 900 RPM passing through reverse flow.

sensor locations are non-dimensionalized by different chords, i.e. c_g = 5 in. for the chordwise direction and c_e = 5.77 in. for the streamwise direction. Chordwise pressure readings were analyzed in the unyawed case, and streamwise pressure readings were analyzed in the yawed case. Pressure transducer data was collected at a Reynolds number of Re = 1.0 x 10^5 and phase-averaged over 120 complete pitching cycles.

2.2 Data Processing

Stereoscopic PIV images were processed using DaVis v8.2.3 by LaVision Inc. Velocity fields were calculated in a multi-pass cross-correlation process, with a minimum window size of 24 x 24 pixels and a 50% overlap between interrogation windows, resulting in a 189 x 110 grid of velocity vectors for each image. The velocity fields fields were phase-averaged over 10 complete pitching cycles with at least 150 images taken per cycle. For clarity, all velocity field figures show 1/6 of the total number of vectors in the x/c and z/c directions. In each of the phase-averaged velocity fields, the spatial position of a vortex core was determined using the Γ_1 vortex tracking methodology outlined by Graftieaux [16], wherein vortex cores are identified by peaks in local rotation. In both the yawed and unyawed configurations, the RFDSV was well-tracked once it had convected past the airfoil mid-chord.

2.3 Parameter Space

To allow for comparison with forward flow dynamic stall data, the model rotor blade was pitched sinusoidally in both the yawed and unyawed configurations, with kinematics chosen carefully to match the unsteadiness on a full-scale high advance ratio rotor. The present work considers only a single mean pitch angle, $\alpha_{\text{rev},0}$ = 10.75°, and a single pitch amplitude, $\alpha_{\text{rev},1}$ = 10.75° but several reduced frequencies. Figure 5 plots these pitch kinematics versus non-dimensional cycle time for a representative frequency. A perfect sinusoidal fit is overlain as a solid black line, with the experimental pitch kinematics showing little variation from a perfect sinusoid.

In conventional dynamic stall experiments, a rotor blade's pitching kinematics are largely governed by the reduced frequency k, a quantity described as a measure of flow unsteadiness and defined by Equation 2.

$$k = \frac{\pi f c}{V_{loc}} \tag{2}$$

In forward flow dynamic stall experiments, reduced frequency can be intuitively related to a full-scale rotor blade, as the pitch frequency f is a consequence of the 1/rev cyclic pitch control on the rotor. The reverse flow region, however, encompasses only a portion of a blade element's revolution, meaning the pitching kinematics within the reverse flow region more closely resemble a linear ramp up than a sinusoidal pitch [7]. A more general measure of flow unsteadiness, the reduced time s, is often employed to characterize unsteadiness in the reverse flow region, and is defined in Equation 3 as the number of semi-chords traveled during a pitch motion of arbitrary shape. Note that Equation 3 includes velocity as a function of time, accounting for the time varying free stream as a blade element passes through the reverse flow region.

$$s = \frac{2}{c}\int_0^t V(t)\,dt \tag{3}$$

Figure 6 shows the radial distribution of reduced time for blade elements passing through the reverse flow region. A rotor radius of 33.5 in, a chord of 3.15 in, and an angular velocity of 900 RPM were assumed in constructing Figure 6, consistent with the values employed in past Mach-scale high-advance ratio rotor experiments at the University of Maryland [3, 4]. For the sinusoidal pitching in the present work, the rotor's reduced time was converted to an "effective" reduced frequency by matching the unsteadiness predicted in Figure 6 to the "pitch up" portion of the sinusoidal pitching cycle. The transformation between reduced time and effective reduced frequency is then governed by Equation 4.

$$k = \pi/s \tag{4}$$

Using the same rotor parameters, Figure 7 shows the radial distribution of effective reduced frequency for blade elements passing through the reverse flow region at $\mu = 0.6$ and $\mu = 1.0$. The present work considers blades pitching at four reduced frequencies within 0.16 $< k <$ 0.45. Each reduced frequency is represented by a solid black dot in Figure 7. For μ = 0.6, these reduced frequencies align with inboard regions of the rotor, where dynamic pressure is highest in reverse flow [1]. For μ = 1.0, these reduced frequencies represent a large sweep of radial locations from r/R = 0.4 to r/R = 0.7.

3. RESULTS

This section explores the impact of yaw on reverse flow dynamic stall in three separate parts. First, Section 3.1 and Section 3.2 outline the basic flow morphology of the flow over a pitching rotor blade in the unyawed and yawed configuration, identifying dominant and secondary flow structures in each case. Second, Section 3.3 compares the convection of the primary dynamic stall vortex in the yawed and unyawed configurations. Finally, Section 3.4 compares the degree of spanwise flow in the yawed and unyawed cases. The outcome of the results shown here is a physical understanding of the formation and convection of the RFSDV in unyawed and yawed flow informed by two dimensional and three dimensional flow fields.

3.1 Unyawed Flow Morphology

As an introduction to the flow features associated with reverse flow dynamic stall, this section outlines the overall flow morphology for a baseline pitching case in the unyawed configuration, Λ_{rev} = 0°. The baseline pitching case is defined as follows: k = 0.217, $\alpha_{0,\mathrm{rev}}$ = 10.75°, and $\alpha_{1,\mathrm{rev}}$ = 10.75°. Recall that one pitching "cycle" is defined as a complete sinusoidal pitch up and pitch down, and the results presented here are phase-averaged over 10 cycles (PIV) or 120 cycles (pressure). Chordwise distance in this configuration is non-dimensionalized by the geometric chord, c_{g} = 5 in.

Figure 8a presents phase-avergaed two-component velocity fields for the unyawed configuration at k = 0.217. In this figure, non-dimensional chordwise position is plotted on the abscissa, non-dimensional vertical position is plotted on the ordinate, and the velocity vectors are overlaid on contours of non-dimensional vorticity. At t/T = 0.40, Figure 8a shows that a region of high magnitude, negative vorticity begins to form near the airfoil's sharp aerodynamic leading edge, corresponding with the rollup of nearby velocity vectors. By t/T = 0.5, the region of vorticity has rolled up into a coherent reverse flow dynamic stall vortex, located at approximately x/c = 0.7. By t/T = 0.6, the RFDSV has convected to the airfoil's blunt trailing edge. In Figure 8a, yellow markers denote the vortex core as calculated by the Γ_1 function. The Γ_1 marker strongly correlates with the visual center of the circular flow region, successfully tracking the RFDSV center in its convection from the midchord to the blunt trailing edge.

As the RFDSV convects along the airfoil chord in the unyawed configuration, it leaves its signature in the unsteady pressure transducer measurements. For the unyawed configuration, Figure 8b shows pressure time histories at k = 0.217 for the 7 sensors installed in the chordwise section of the blade. Non-dimensional cycle time is plotted on the abscissa, and pressure coefficient C_{P}, adjusted here to visually space out the sensor time histories, is plotted on the ordinate. Each pressure time history begins at a

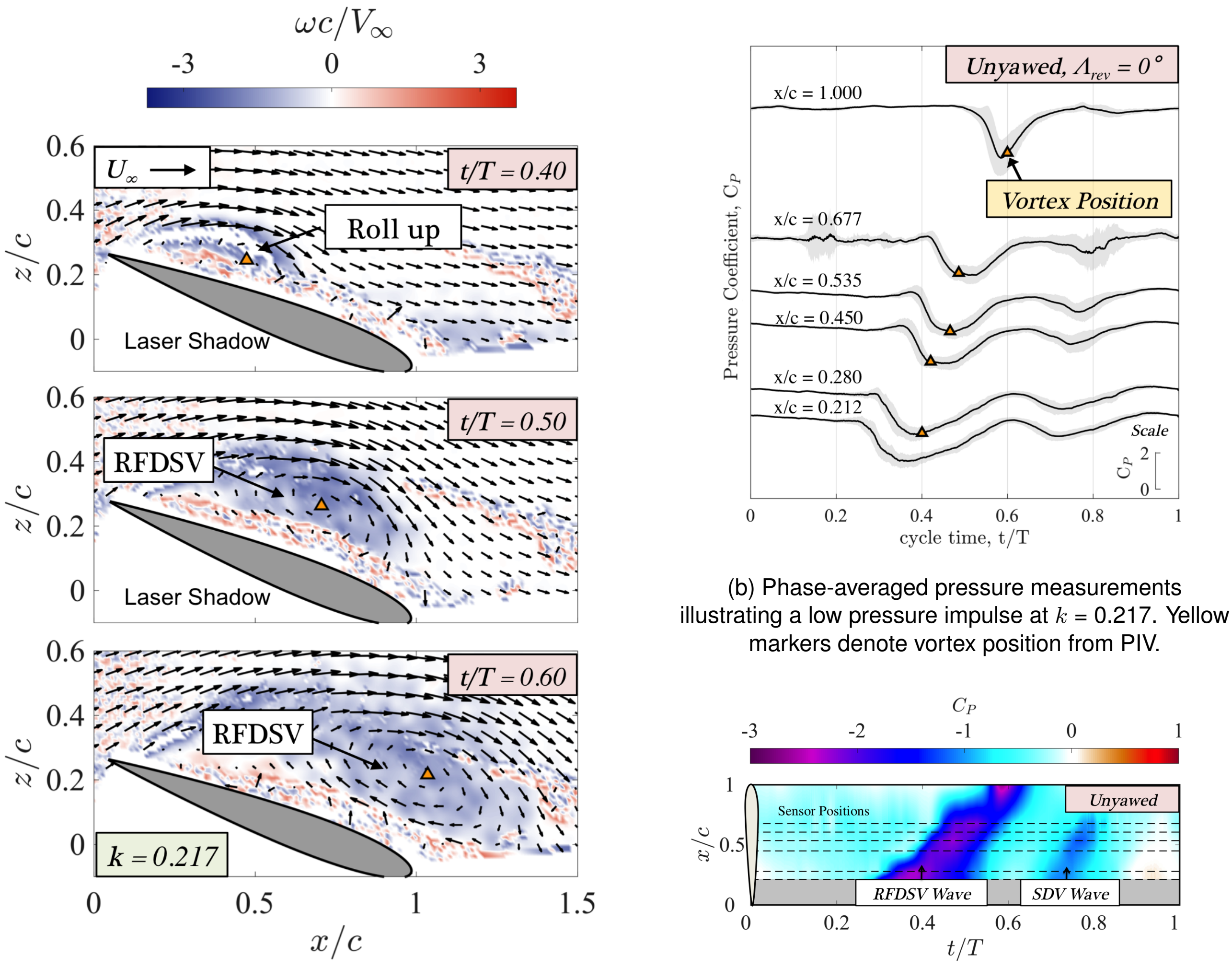

(a) Phase-averaged PIV showing a reverse flow dynamic stall vortex (RFDSV) in the unyawed configuration at k = 0.217

(b) Phase-averaged pressure measurements illustrating a low pressure impulse at k = 0.217. Yellow markers denote vortex position from PIV.

(c) Phase-averaged pressure contour illustrating convection of an RFDSV and a secondary vortex (SDV) at k = 0.217.

Fig. 8: Flow morphology of the unyawed configuration (Λ_{rev} = 0°) at k = 0.217, showing the development of a dynamic stall vortex about the sharp leading edge. The pressure sensors also detect a strong secondary vortex.

starting pressure coefficient near $C_{\text{P}} \approx 0$, and the vertical spacing of each time history is scaled according to x/c. The grey outline around each time history represents two standard deviations away from the solid phase-averaged line.

In Figure 8b, consider first a single pressure transducer, say the sensor at x/c = 0.280. Here, the pressure remains fairly constant for $0 < t/T < 0.3$, after which the pressure begins to rapidly decrease, reaching a minimum near t/T = 0.4. This large negative spike in pressure is visible in each successive sensor along the chord; however, as chord location x/c increases, the large negative spike occurs at later times in the pitch cycle. The large negative spike in pressure is the signature of the RFDSV as it convects along the airfoil surface. The yellow markers in Figure 8b represent points in PIV vortex tracking at which the vortex reaches the x/c position of each sensor. The markers show that vortex tracking is aligned with the large negative spike in pressure. The similarity in vortex position with pressure spike persists even though the PIV was collected at a significantly lower Reynolds number than the pressure readings.

As a final way of visualizing the flow structures in the unyawed configuration, Figure 8c presents contours of pressure coefficient C_{P} over the entire pitch cycle at k = 0.217. Non-dimensional cycle time is plotted on the abscissa and non-dimensional chordwise position is plotted on the ordinate. The dark blue regions in Figure 8c correspond to regions of very low pressure coefficient. Similar to the pressure time histories, the pressure contour reveals a low pressure region that appears on the chord near t/T = 0.3 before spreading along the chord over $0.3 < t/T <$

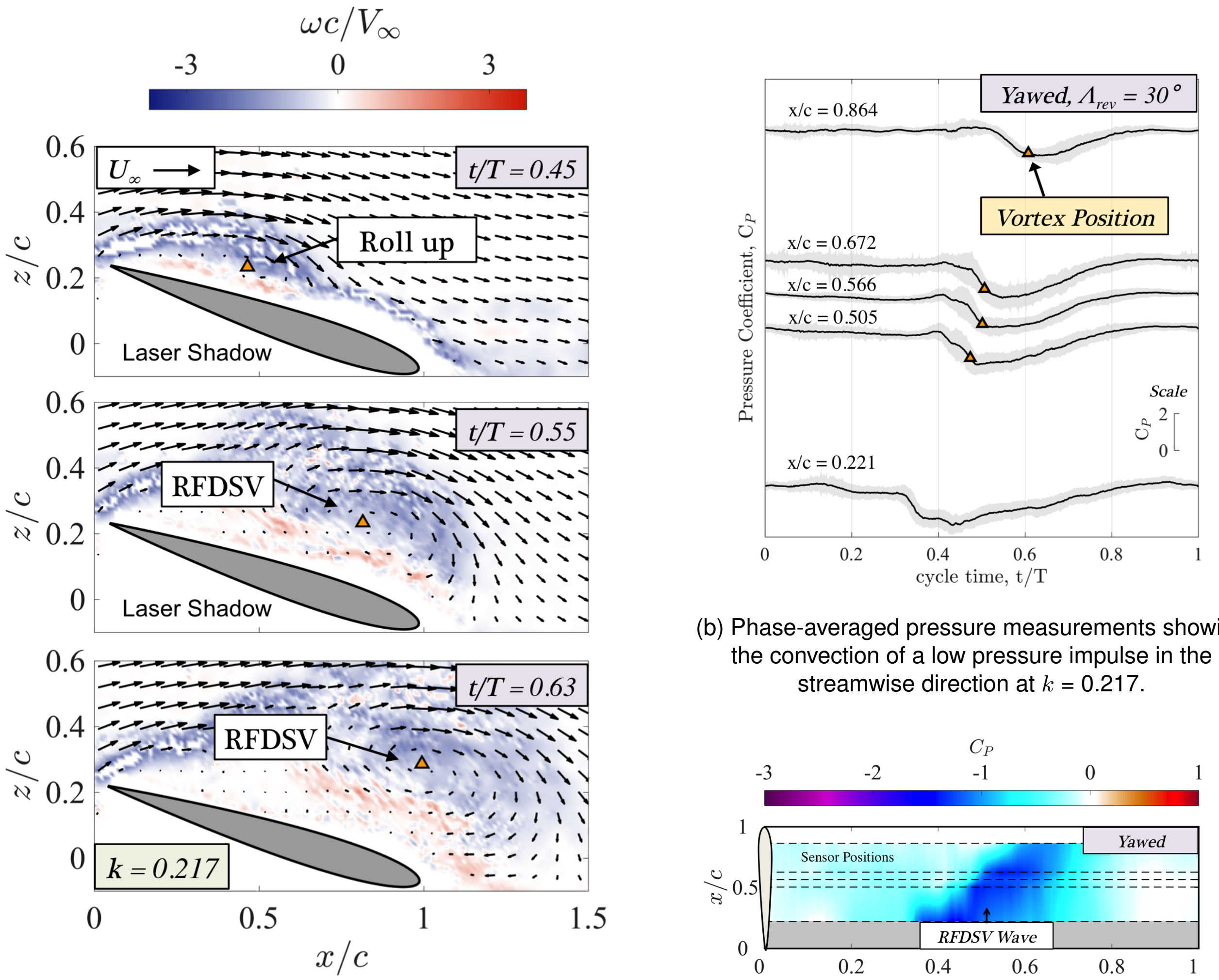

(a) Phase-averaged PIV showing a reverse flow dynamic stall vortex (RFDSV) in the yawed configuration at k = 0.217

(b) Phase-averaged pressure measurements showing the convection of a low pressure impulse in the streamwise direction at k = 0.217.

(c) Phase-averaged pressure contour illustrating convection of low pressure impulse at k = 0.217.

Fig. 9: Flow morphology of the yawed configuration (Λ_{rev} = 30°) at k = 0.217, showing the development of a dynamic stall vortex in the streamwise direction. Note the absence of significant secondary flow structures.

0.55. This initial low pressure wave corresponds to the RFDSV. Figure 8c also shows a weaker low pressure region near t/T = 0.7, suggesting the presence of a secondary vortex.

In summary, time-resolved PIV showed that the unyawed configuration at k = 0.217 results in a dominant RFDSV, forming near the sharp leading edge and inducing a low pressure wave as it convects along the chord. A weaker secondary vortex appears shortly following the convection of the RFDSV. These results are consistent with prior work on unyawed blades in reverse flow at comparable reduced frequencies [6].

3.2 Yawed Flow Morphology

Expanding upon the discussion above, this section provides an overview of the flow morphology for a baseline pitching case in the yawed configuration, Λ_{rev} = 30°. Again, the baseline pitching case is defined as k = 0.217, $\alpha_{0,\text{rev}}$ = 10.75°, and $\alpha_{1,\text{rev}}$ = 10.75°. Recall that in the yawed configuration, pressure and velocity field measurements are taken in the streamwise direction, meaning the effective chord is larger than the geometric chord (Figure 3). For Λ_{rev} = 30°, the effective chord is equal to c_e = 5/cos(30°) = 1.15 c_g

Figure 9a presents time-resolved, phase-averaged velocity fields for the yawed configuration at k = 0.217. In this figure, non-dimensional streamwise position is plotted on the abscissa, while non-dimensional vertical position is plotted on the ordinate. The velocity vectors are again overlaid on a contour of non-dimensional vorticity, with blue representing negative vorticity and red representing positive vorticity. Figure 9a reveals that at k = 0.217 flow structures

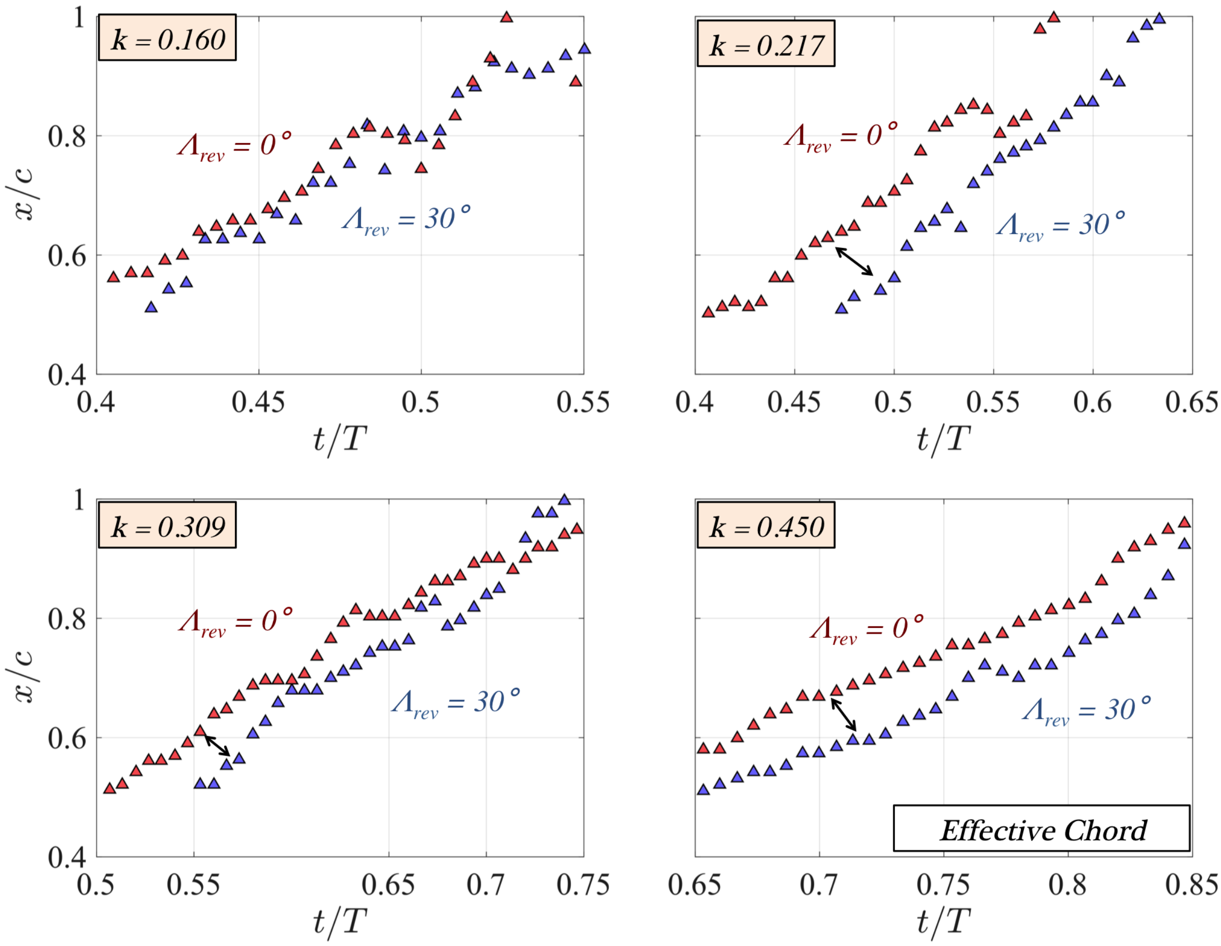

Fig. 10: Vortex center on blade surface as calculated from local maxima in the Γ_1 function. The results here are non-dimensionalized by the geometric chord in the unyawed case (c_g = 5 in) and the effective chord in the yawed case (c_e = 5.77 in)

develop very similarly in the yawed configuration to the unyawed configuration. At t/T = 0.45, a region of negative vorticity appears near the sharp leading edge, and the velocity vectors begin to roll up. By t/T = 0.55, a coherent RFDSV is located near the three-quarter chord, and by t/T = 0.63, the RFDSV has reached the model's blunt trailing edge. Despite the blade being yawed, a RFDSV still forms and convects in a plane parallel to the freestream.

The PIV results show that an RFDSV forms for both the yawed and unyawed configurations a RFDSV. Unsteady pressure measurements suggest two differences in flow morphology between the two configurations. First, consider the pressure sensor time histories plotted in Figure 9b for the yawed configuration. In this figure, non-dimensional cycle time is plotted on the abscissa, and adjusted pressure coefficient is plotted on the ordinate. The pressure coefficient time histories again show a negative spike in pressure coefficient that is delayed to later times in the cycle at successive sensor locations along the chord. However, the magnitude of the negative spikes is substantially lower compared to the pressure spike induced in the unyawed configuration.

The lower magnitude pressure wave is reflected in Figure 9c, which shows a pressure contour for the yawed configuration at k = 0.217. In this plot, non-dimensional cycle time is plotted on the abscissa, streamwise position is plotted on the ordinate, and dark blue regions again correspond to regions of large negative pressure coefficient. Just as in the unyawed case, Figure 9c reveals a low pressure wave near t/T = 0.3 that convects from the sharp leading edge to the blunt trailing edge. However, the magnitude of the low pressure wave is reduced, as the low pressure region is qualitatively a lighter shade of blue than the corresponding wave in the unyawed configuration. Perhaps more significantly, the low pressure signature of a secondary vortex is completely absent from the yawed configuration pressure contour in Figure 9c, suggesting that yaw hinders the development of secondary vortex structures.

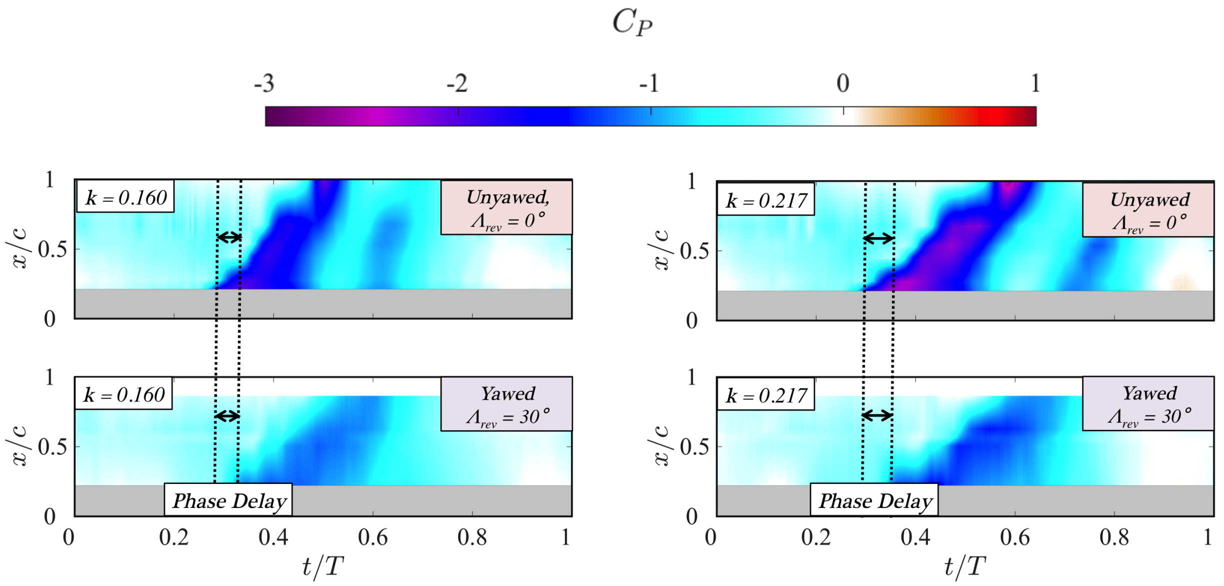

Fig. 11: Phase-averaged pressure contours illustrating the delayed onset of a low pressure impulse in the yawed configuration when non-dimensionalized by the effective chord

In summary, the yawed configuration at k = 0.217 results in a RFDSV that convects from the sharp leading edge to the blunt trailing edge, leaving a low pressure impulse as it convects. The magnitude of the low pressure impulse is significantly less in the yawed case than the unyawed case, and the presence of yaw appears to hinder the development of secondary flow structures. These latter two results are also observed when adding yaw to a model in forward flow dynamic stall [17].

3.3 Unyawed - Yawed Comparison: Vortex Tracking

The previous two sections identified an RFDSV when the flow is both yawed and unyawed. This section more closely compares the convection behavior of the primary vortex in each configuration. For a sweep of reduced frequencies, the RFDSV was tracked as it convected from the airfoil midchord to the blunt trailing edge, based on results of the Γ_1 function. The vortex core was unable to be identified earlier in the cycle due to limitations in the Γ_1 function and the field of view of the cameras. Recall that in the results below, vortex position measurements are presented in the chordwise direction for the unyawed case but in the streamwise direction in the yawed case. However, both the chordwise and streamwise directions are aligned with the freestream.

Figure 10 shows the results of vortex tracking for the unyawed and yawed configurations over a sweep of reduced frequencies, 0.16 $< k <$ 0.45. In these figures, a portion of the non-dimensional cycle is plotted on the abscissa, and position along the chord is plotted on the ordinate. Keep in mind that for the yawed condition, vortex positions are normalized by the effective chord (c_e = 5/cos(30°) in.), and in the unyawed condition, vortex positions are normalized by the geometric chord (c_g = 5 in.). Figure 10 reveals an important observation: across all tested reduced frequencies, the speed of the vortex convection does not appear to be affected by the addition of yaw. That is, the "slope" of each plot in Figure 10 is very similar both the unyawed and yawed configuration. This similarity in convection in reverse flow is at odds with classic results from forward flow dynamic stall, where a yawed blade is associated with reduced convection speed of the dynamic stall vortex [12, 13].

Figure 10 does, however, reveal a phase lag in RFDSV position across 0.217 $< \; k \; <$ 0.450. In the k = 0.217 case, for instance, the unyawed vortex reaches x/c = 0.6 at t/T = 0.45, but the yawed vortex does not reach x/c = 0,6 until t/T = 0.5, suggesting the yawed vortex lags behind the unyawed vortex. A similar phase shift is noticed when comparing pressure contours for each configuration. Figure 11 gives chordwise and streamwise pressure contours for the unyawed and yawed configurations, respectively, showing a delay of the appearance of the low pressure wave across two reduced frequencies. However, keep in mind that the unyawed and yawed results are non-dimensionalized by different chords. That is, the position x/c = 0.5 represents a different point in physical space in the unyawed condition compared to the yawed condition.

To address the idea of differing effective chords, Figure 12 plots the vortex tracking results normal-

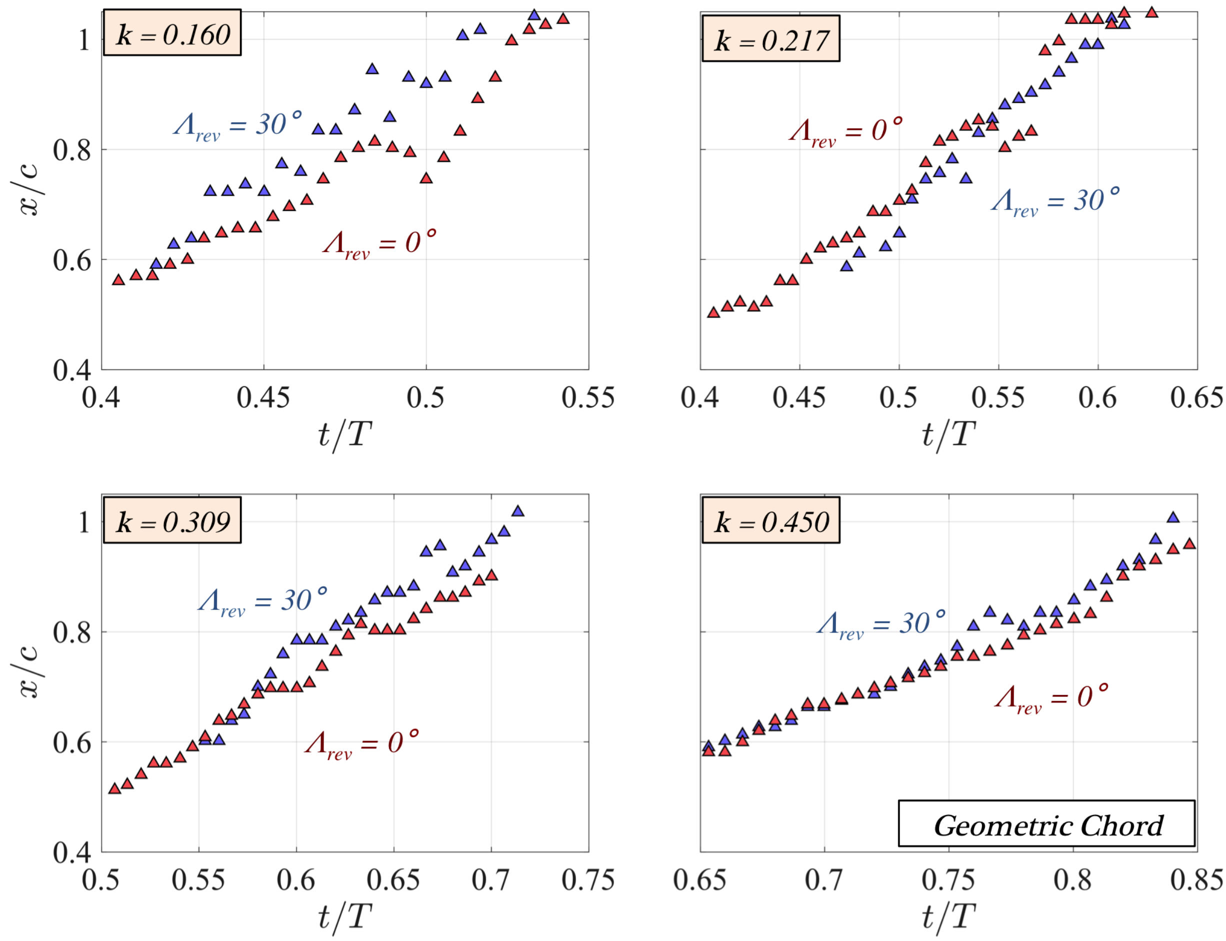

Fig. 12: Vortex center on blade surface as calculated from local maxima in the Γ_1 function. The results here are non-dimensionalized by the *geometric* chord, 5 in for both cases. Note the similarity between the yawed and unyawed cases.

ized by the same chord, the geometric chord. Non-dimensional cycle time is again plotted on the abscisa, and vortex position is plotted on the ordinate. Here, a value of x/c = 0.5 represents the same point in physical space in both the yawed and unyawed configurations. Figure 12 reveals that when non-dimensionalized by the same chord, the vortex positions collapse onto one another, eliminating the phase delay seen previously. Across 0.217 $< k <$ 0.450, the RFDSV appears to take a very similar path in the direction of the freestream despite the presence of yaw. This idea is illustrated more clearly in Figure 13. Here, the colored dots represent yawed and unyawed vortex positions at two different times, t/T = 0.57 and t/T = 0.82, and are overlaid on sketches of the blade in both the yawed and unyawed positions. At the same point in the pitch cycle, the unyawed and yawed vortices are located at the same physical distance from the sharp leading edge, the only difference is the yawed configuration features a longer effective chord.

In summary, RFDSV positions have been compared in the direction of the freestream for the yawed and unyawed configuration. Contrary to classic results in forward flow, yaw appears to have little impact on the convection speed of the RFDSV. When non-dimensionalized by the same chord, unyawed and yawed vortex positions prove to be very similar in time, suggesting the vortices convect very similarly in physical space. The only difference is that the yawed configuration has a longer effective chord, meaning the vortex impacts the blade for a longer period in the yawed configuration.

3.4 Unyawed-Yawed Comparison: Spanwise Flow

As a final result, this section quantifies the amount of spanwise flow in unyawed and yawed planar velocity fields, focusing on spanwise flow near the RFDSV. Spanwise flow measures the degree of three-dimensionality in flow structures and is comparable to radial flow on a spinning rotor. The overall goal of this section is to make fundamental observations regard-

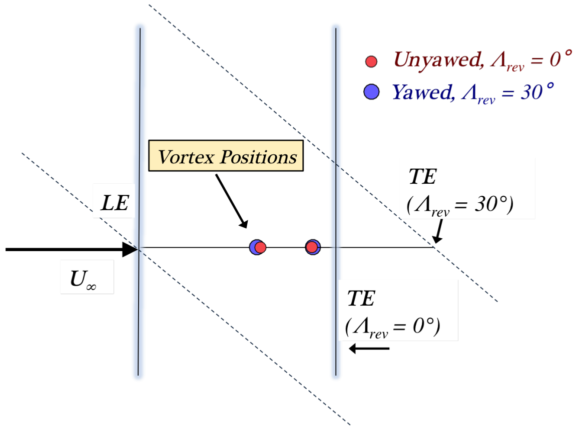

Fig. 13: Diagram of the yawed and unyawed vortex convection in physical space. For each yaw configuration, two vortex positions (t/T = 0.67 and t/T = 0.82) are plotted along the effective chord. Note that the convection of the vortex is very similar for both cases. The yawed configuration simply has a longer effective chord.

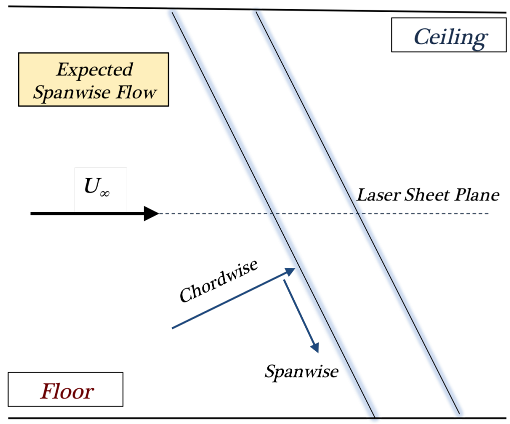

Fig. 14: Diagram illustrating the expected spanwise flow direction for a yawed blade at static conditions. Because the blade chord direction is tilted "upward" in the yawed configuration, the freestream velocity vector can be decomposed into a chordwise component and spanwise component directed toward the floor.

ing the spanwise flow component in the unyawed and yawed conditions, working towards a more complete picture of the RFDSV's behavior in three dimensional space.

Note that in the case of attached flow at static yaw angles, the direction of spanwise flow can be predicted by decomposing the freestream velocity vector into a chordwise component and a spanwise component. Figure 14 illustrates this idea, showing that in the present work, spanwise flow is expected to travel downward, toward the wind tunnel floor, when the blade is yawed. In the discussion that follows, the direction of spanwise flow will be carefully compared to the expected direction of spanwise flow under static conditions. Hence, this section will also judge whether the expected directions of spanwise flow, predicted based on static yaw angles and static pitch angles, holds when the blade is undergoing dynamic pitching.

Figure 15 shows the phase-averaged development of spanwise flow in the yawed and unyawed configurations at k = 0.450. In each figure, non-dimensional streamwise position is plotted on the abscissa, non-dimensional vertical position is plotted on the ordinate, and the two-component velocity vectors (in plane with the laser sheet) are overlaid on contours of the third component of the velocity field (out of plane with the laser sheet). Here, a dark red region corresponds to spanwise flow toward the tunnel floor, the expected direction of spanwise flow, and a dark blue region corresponds to spanwise flow toward the tunnel ceiling, a direction opposite from the expected. Note that at high pitch angles in the yawed condition, the upstream camera is blocked from viewing the blade surface, preventing the third components of velocity from being resolved in this region. The k =0.450 case was chosen because the RFDSV largely convects during the "pitch down" portion of the cycle, allowed for optimal optical access to the RFDSV vortex core during its convection.

First, consider spanwise flow in the yawed configuration seen in the left-hand portion of Figure 15. At t/T = 0.60, the RFDSV has just begun rolling up about the sharp leading edge, and the highest magnitude of spanwise flow, located above the vortex core, is in the direction predicted by static assumptions (red). Near the vortex core at x/c = 0.4, however, a significant amount of spanwise flow is directed toward the wind tunnel ceiling, a direction opposite of what is predicted under static conditions. This flow structure is more developed by t/T = 0.75, where a very high magnitude of spanwise flow is centered at the vortex core and oriented toward the tunnel ceiling. By t/T = 0.90, the upward-directed spanwise flow covers the entire suction surface of the blade, corresponding with the departure of the RFDSV from the blade surface. Note that portions outside the vortex core, away from the blade surface, appear to be predominately convecting in the direction predicted by static conditions.

Next, consider spanwise flow in the unyawed configuration seen in the right-hand portion of Figure 15. Across all times in the pitch cycle, the unyawed configuration appears to have a substantially lower magnitude of spanwise flow than the corresponding yawed fields. The unyawed configuration still results in a non-negligible amount of spanwise flow, particularly near the vortex core, but the trends in spanwise flow direction are much less predictable over time. At t/T = 0.60 and t/T = 0.75, for instance, spanwise flow is directed toward the tunnel ceiling near the RFDSV core, with spanwise flow directed at the floor near the edges of the vortex. By t/T = 0.90, however, the directions have switched, and spanwise flow is directed toward the floor at the vortex center. Keep in mind that in the unyawed configuration under static conditions, spanwise flow is not predicted to travel toward the tunnel ceiling or the floor. The presence of spanwise flow may be a consequence of the end wall boundary condition, a limitation in low speed wind tunnel testing shown to introduce spanwise variations in dynamic stall vortex structure on aspect ratio 4 model blades [18].

In summary, the yawed case at k = 0.450 produces a significantly larger magnitude of spanwise flow than the unyawed case at k = 0.450. Far from the vortex core, the yawed case produces spanwise flow in the direction predicted by static assumptions, but near the vortex core, spanwise flow is in the opposite direction. The unyawed case produces a non-negligible amount of spanwise flow, but the trends in spanwise flow direction are much less consistent over time than the yawed case.

4. CONCLUSIONS

The reverse flow dynamic stall vortex is the dominant flow feature associated with the reverse flow region of a high-advance ratio rotor. In an effort to model the large torsional loads incurred by the reverse flow dynamic stall vortex, experimental work has sought to develop a physical understanding of the behavior of this flow structure. The present work addresses the influence of yaw on the formation and convection of the reverse flow dynamic stall vortex. A subscale rigid model rotor blade was held at two static yaw angles in reverse flow, Λ_{rev} = 0° and Λ_{rev} = 30°, and was dynamically pitched about its geometric quarter-chord. Dynamic pitching was completed for a single set of pitch kinematics over a sweep of reduced frequencies from k = 0.160 to k = 0.450. Three-component velocity fields were obtained from stereoscopic particle image velocimetry, and surface pressure time histories were obtained using discrete unsteady pressure transducers installed at positions along the suction surface of the model. The resulting analyses led to the following conclusions:

- The presence of yaw still results in a reverse flow dynamic stall vortex in the direction of the freestream that induces a low pressure impulse as it convects along the effective chord of the rotor blade.
- Reverse flow dynamic stall remains fairly insensitive to Reynolds number, as vortex positions taken at Re = 2.5 x 10^4 closely align with pressure impulses at Re = 1.0 x 10^5.
- The presence of yaw appears to weaken the magnitude of the RFDSV low pressure impulse and hinder the development of secondary flow structures.
- In the direction of the freestream, the presence of yaw does not have a noticeable effect on the convection speed or timing of the RFDSV in physical space.
- The presence of yaw significantly increases the magnitude of spanwise flow along the blade. When the blade is yawed, the direction of spanwise flow is consistent with static yaw assumptions away from the vortex core but is in the opposite direction near the vortex core.

This experimental study lays the groundwork for a physical understanding of the complete, three-dimensional convection behavior of the reverse flow dynamic stall vortex. Future work will expand on the present conclusions in three ways: evaluating the present conclusions at a wider range of yaw angles, investigating the impact of yaw on unsteady chordwise airloads in reverse flow, and exploring spanwise variations in planar flow morphology. Coupled with results from full-scale and Mach-scale rotor tests, this work will contribute to the development of a predictive model for the impact of the reverse flow dynamic stall vortex on the aerodynamics of high advance ratio rotors.

5. ACKNOWLEDGEMENTS

This work was supported by the U.S. Army/Navy/NASA Vertical Lift Research Center of Excellence Cooperative Agreement with Mahendra Bhagwat serving as Program Manager and Technical Agent, grant number W911W6-17-2-0004. The authors wish to acknowledge Jonathan Lefebvre and Peter Mancini for their patience, advice, and assistance throughout the wind-tunnel experiments.

6. COPYRIGHT STATEMENT

References

[1]Leishman, J., *Principles of Helicopter Aerodynamics*, Cambridge University Press, second edition, 2006.

[2]Datta, Y. H., A. and Norman, T., "Experimental Investigation and Fundamental Understanding of a Full-Scale Slowed Rotor at High Advance Ratio," *Journal of the American Helicopter Society*, Vol. 58, January 2013.

[3]Berry, B. and Chopra, I., "Slowed Rotor Wind Tunnel Testing of an Instrumented Rotor at High Advance Ratio," , September 2014.

[4]Berry, B. and Chopra, I., "High Advance Ratio Wind Tunnel Testing of a Model Rotor with Pressure Measurements," , January 2014.

[5]Harris, F., "Rotor Performance at High Advance Ratio," NASA CR 215370, 2008.

[6]Lind, A. H. and Jones, A. R., "Unsteady Aerodynamics of Reverse Flow Dynamic Stall on an Oscillating Blade Section," *Physics of Fluids*, Vol. 28, (7), Jul. 2016, pp. 1–22.

[7]Smith, L., Lind, A. H., Jacobson, K., Smith, M. J., and Jones, A. R., "Experimental and Computational Investigation of a Linearly Pitching NACA 0012 in Reverse Flow," 72nd Forum of the AHS, May 2016.

[8]Gormont, R., "A mathematical model of unsteady aerodynamics and radial flow for application to helicopter rotors," USAA MRDL 72-67, May 1973.

[9]Purser, P. and Spearman, M., "Wind-Tunnel Tests at Low Speed of Swept and Yawed Wings Having Various Plan Forms," NACA TN 2445, 1951.

[10]Harris, F., "Preliminary Study of Radial Flow Effects on Rotor Blades," *Journal of the American Helicopter Society*, Vol. 11, (3), 1966, pp. 121.

[11]St Hilaire, C. F. F. M., A. and Jepson, W., "Influence of Sweep on the Aerodynamic Loading of an Oscillating NACA0012 Airfoil," NASA CR 3092, 1979.

[12]St Hilaire, A. and Carta, F., "Analysis of Unswept and Swept Wing Chordwise Pressure Data from an oscillating NACA0012 experiment," NASA CR 3567, 1983.

[13]Leishman, J., "Modeling Sweep Effects on Dynamic Stall," *Journal of the American Helicopter Society*, July 1989.

[14]Hodara, J. and Smith, M., "Improvement of Crossflow Aerodynamic Prediction for Forward Flight at All Advance Ratios," 40th European Rotorcraft Forum, September 2014.

[15]Modarres, R. and Peters, D., "Modeling the Effect of Yawed Flow on Dynamic Stall with Secondary Lift Peak - Experimental Correlation," , May 2016.

[16]Graftieaux, M. M., L. and Grosjean, N., "Combining PIV, POD and Vortex Identification Algorithms for the Study of unsteady Turbulent Swirling Flows," *Measurement Science and Technology*, Vol. 12, (9), 2001.

[17]Salari, K. and Roache, P., "The Influence of Sweep on Dynamic Stall Produced by a Rapidly Pitching Wing," , January 1990.

[18]Visbal, M. and Garmann, D., "Numerical Investigation of Spanwise End Effects on Dynamic Stall of a Pitching NACA 0012 Wing," 55th AIAA Aerospace Sciences Meeting, January 2017.

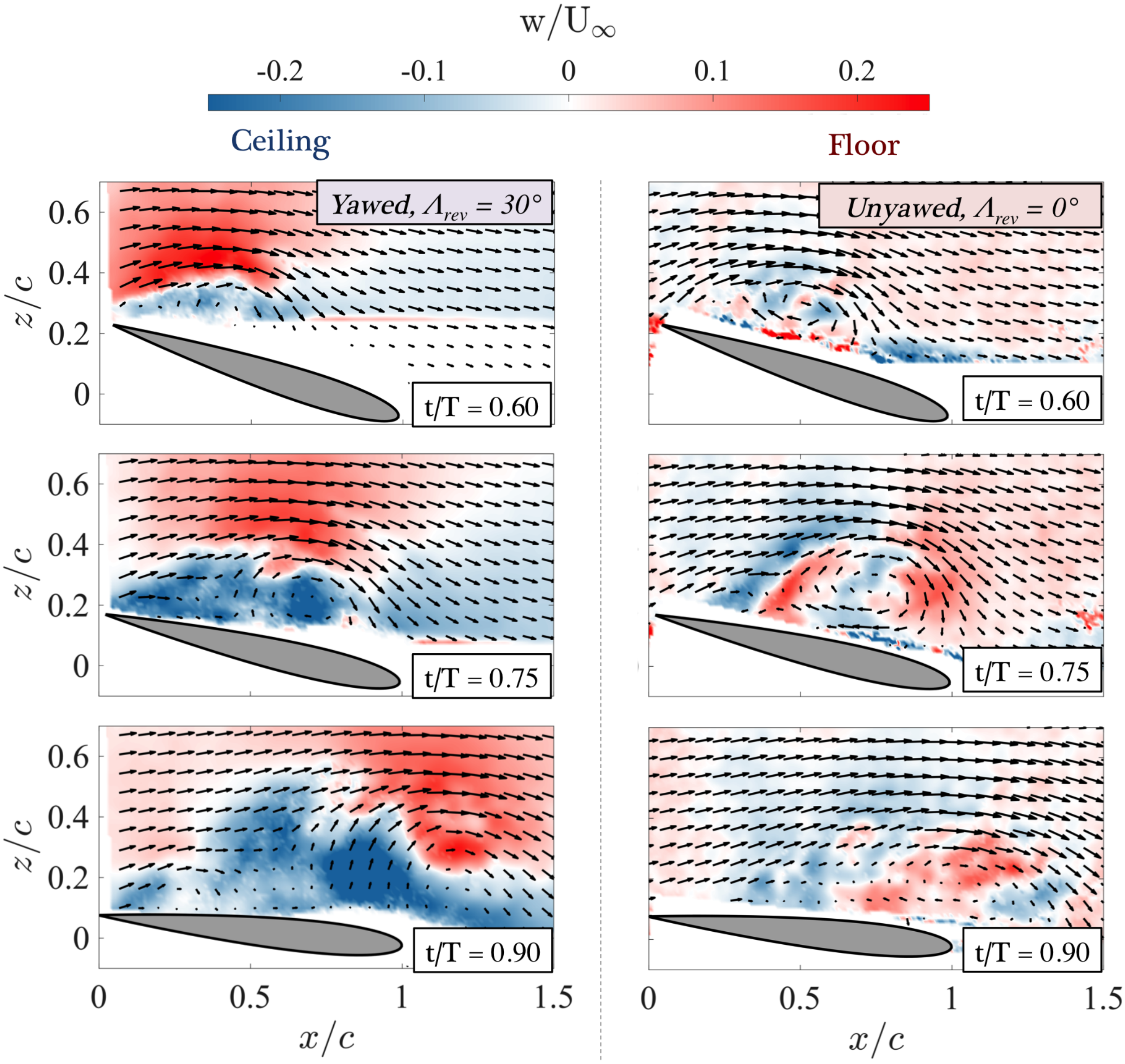

Fig. 15: Phase-averaged vector fields showing contours of spanwise flow for the yawed (left) and unyawed (right) conditions at k = 0.450. Red regions correspond to flow toward the tunnel floor (the expected direction), while blue represents flow toward the tunnel ceiling. Note the significant increase in spanwise flow in the yawed configuration, particularly near the vortex core.